European Journal of Mechanics / A Solids 75 (2019) 322–329

Contents lists available at ScienceDirect

European Journal of Mechanics / A Solids

journal homepage: www.elsevier.com/locate/ejmsol

Numerical analysis of periodic laminar and fibrous media undergoing a jamming transition

Nikolaos Vasios[a], Yashraj Narang[a], Buse Aktaş[a], Robert Howe[a], Katia Bertoldi[a,b,*]

[a] Harvard John A. Paulson School of Engineering and Applied Sciences, Harvard University, Cambridge, MA, 02138, United States
[b] Kavli Institute, Harvard University, Cambridge, MA, 02138, United States

ARTICLE INFO

Keywords:
Jamming transition
Finite element analysis
Layers
Fibers
Tunable stiffness

ABSTRACT

Materials capable of dramatically changing their stiffness along specific directions in response to an external stimulus can enable the design of novel robots that can quickly switch between soft/highly–deformable and rigid/load–bearing states. While the jamming transition in discrete media has recently been demonstrated to be a powerful mechanism to achieve such variable stiffness, the lack of numerical tools capable of predicting the mechanical response of jammed media subjected to arbitrary loading conditions has limited the advancement of jamming-based robots. To overcome this limitation, we introduce a 3D finite–element-based numerical tool that predicts the mechanical response of pressurized, infinitely–extending discrete media subjected to arbitrary loading conditions. We demonstrate the capabilities of our numerical tool by investigating the response of periodic laminar and fibrous media subjected to various types of loadings. We expect this work to foster further numerical studies on jamming–based soft robots and structures by facilitating their design, as well as providing a foundation for combining various types of jamming media to create a new generation of tunable composites.

1. Introduction

Highly deformable materials have recently enabled the design of a new class of soft robots that, in contrast to their rigid counterparts, are adaptive, resilient and safe for human interaction (Trivedi et al., 2008; Ilievski et al., 2011; Shepherd et al., 2011; Kim et al., 2013a; Majidi, 2014; Rus and Tolley, 2015; Laschi et al., 2016; Zhao et al., 2016; DianV. M. S et al., 2016; Polygerinos et al., 2017). However, the inherent compliance of soft robots is also the source of their greatest drawback, namely their inability to exert large forces on objects without sacrificing complete softness (Manti et al., 2016; Narang et al., 2018a).

Recent studies have shown that jamming is a promising solution to the problem of combining the virtues of rigid and soft robots (Liu and Nagel, 2010; Brown et al., 2010; Narang et al., 2018a; Narang et al., 2018b; Kim et al., 2013b; Ou et al., 2013; Jaeger, 2015; Kawamura et al., 2002). In the unjammed state, an assembly of small objects can flow freely and is very compliant, but upon application of a vacuum, it contracts and hardens quickly (Liu and Nagel, 2010). Such a reversible jamming transition has been exploited in granular media to design universal grippers (Brown et al., 2010) and in laminar structures to realize variable–compliance robots (Narang et al., 2018a; Narang et al., 2018b; Kim et al., 2013b; Ou et al., 2013; Kawamura et al., 2002). However, although several studies have shown the great potential of the jamming phenomenon to inspire the design of more advanced robots, numerical techniques capable of predicting the response of such jamming–based structures are still very limited. For granular media, continuum theories (Henann and Kamrin, 2013, 2014) have been developed and discrete element simulations (Rycroft et al., 2006) have been employed to study dense granular flows. For laminar media nonlinear Finite Element (FE) analyses have been performed to investigate the response of structures subjected to two-point bending (Narang et al., 2018a, 2018b; Narang, 2018). However, there is still no unified numerical tool capable of predicting the response of both laminar, fibrous and granular media undergoing a jamming transition. Such a tool will enable the design of optimized jamming–based robots capable of switching between highly compliant and stiff (almost rigid) states and also provide crucial insights into the working principles of these highly tunable machines.

In this article,[1] we propose a 3D FE-based numerical tool that predicts the mechanical response of discrete infinite media undergoing a jamming transition. In particular, we focus on assemblies of layers and fibers and investigate the mechanical response of representative volume elements under various loading conditions. We find that, in contrast to

* Corresponding author. Harvard John A. Paulson School of Engineering and Applied Sciences, Harvard University, Cambridge, MA 02138, United States.
E-mail address: bertoldi@seas.harvard.edu (K. Bertoldi).

[1] This article represents the plenary lecture given by Katia Bertoldi at the Euromech Solid Mechanics Conference in Bologna, 2018

https://doi.org/10.1016/j.euromechsol.2019.02.002
Received 21 December 2018; Received in revised form 2 February 2019; Accepted 3 February 2019
Available online 19 February 2019
0997-7538/ © 2019 Elsevier Masson SAS. All rights reserved.

granular assemblies (Jaeger, 2015), the stiffness of all considered structures significantly decreases when they are subjected to shear deformations that cause their discrete constituents to slide against each other. This response is manifested by a distinct yield point in the stress–strain curve and is reminiscent of the elastic-plastic response of metallic materials. However, in contrast to metallic materials for which plastic deformation is irreversible, the behavior of our jamming-based structures is fully reversible, and the location of the yield point can be easily tuned by either varying the jamming pressure or the friction coefficient at the interfaces. Finally, we also find that variations in the cross-section of the fibers and their arrangement play an important role and can suppress the yield point.

2. Numerical simulations

All our analyses are performed using the Standard solver of the commercial FE code Abaqus 2017 (Dassault Systèmes) and consist of four steps (the Abaqus Python script files are available online as Supporting Information):

Step A: Creating the model. To begin with, for any given arrangement of layers/fibers, we create a 3D model of a representative volume element (RVE) and mesh it using hybrid linear hexahedral elements (Abaqus element type C3D8H). Note that, to facilitate the analysis and the enforcement of periodic boundary conditions (see Step B), we ensure that the RVE boundary is free of surfaces on which contact is expected and separate all discrete elements by a small distance δ (see Fig. 1a). Next, to avoid the formation of artificial gaps between the discrete components of the RVE that are in contact and to maintain contact continuity throughout the analysis, 26 additional identical copies of the RVE are generated and the 27 cells are arranged on a $3 \times 3 \times 3$ configuration so that the original RVE is fully enclosed at the center of the super-cell (see Fig. 1b). We will hereby refer to the RVE at the center of the super-cell as the "master" RVE and to the 26 surrounding RVEs as "slaves."

Step B: Boundary conditions and constraints. To investigate the response of infinitely extending media, we impose periodic boundary conditions on every node located on the exterior surface of the "master" RVE. In particular, for each pair (a) and (b) of periodically-located nodes on the boundary of the "master" RVE, the displacements $\boldsymbol{u}^{(a)}$ and $\boldsymbol{u}^{(b)}$ are set to satisfy (see Fig. 1c)

$$\boldsymbol{u}^{(a)} - \boldsymbol{u}^{(b)} = (\boldsymbol{F} - \boldsymbol{I})\cdot(\boldsymbol{X}^{(a)} - \boldsymbol{X}^{(b)}) \tag{1}$$

where $\boldsymbol{F}$ is the macroscopic deformation gradient tensor, $\boldsymbol{I}$ represents the identity tensor and $\boldsymbol{X}^{(a)}$ denotes the position of the node (a) in the undeformed configuration.

Furthermore, the deformation field of all 26 "slave" RVEs is set to be identical to that of the "master" RVE. This is achieved by connecting the displacement of each node (c) within a "slave" RVE to that of the corresponding node (d) in the "master" RVE through

$$\boldsymbol{u}^{(c)} - \boldsymbol{u}^{(d)} = (\boldsymbol{F} - \boldsymbol{I})\cdot(\boldsymbol{X}^{(c)} - \boldsymbol{X}^{(d)}). \tag{2}$$

Note that to implement Eqs. (1) and (2), we define 3 virtual points with artificial degrees of freedom, one for each spatial dimension of the problem (Danielsson et al., 2002; Bertoldi and Boyce, 2008). Since each virtual point has 3 degrees of freedom, we use these 9 additional degrees of freedom to fully define the components F_{ij} of the deformation gradient tensor $\boldsymbol{F}$. Finally, since all degrees of freedom of the "slave" RVEs are coupled to those of the "master" RVE via Eq. (2), the actual degrees of freedom of the problem correspond only to those of the "master" RVE.

Step C: Pressurization. Next, we bring the discrete constituents of the RVE to the jammed state by subjecting the model to a hydrostatic stress state $\boldsymbol{s}^{\mathrm{h}} = -p\boldsymbol{I}$, where p is the magnitude of the applied pressure. In all our analyses, the hydrostatic stress is applied directly to the periodic boundary of the "master" RVE, while leaving all degrees of freedom of the virtual points unconstrained. The deformation induced by the

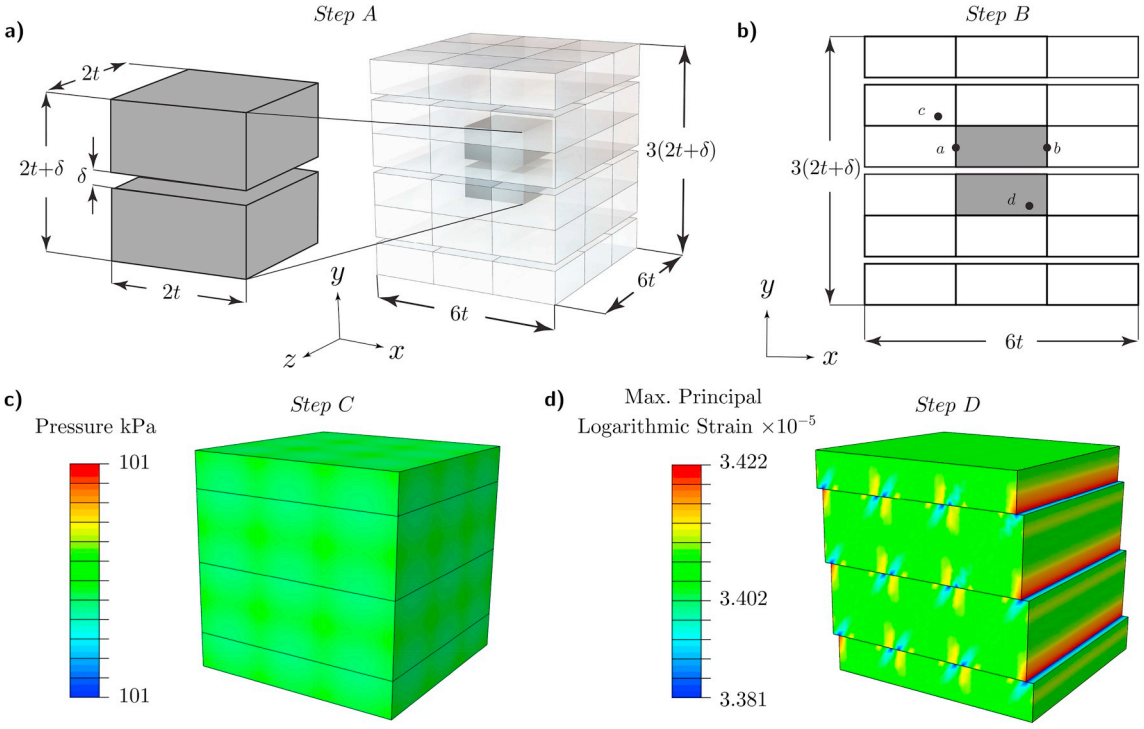

Fig. 1. Numerical simulations. (a) Step A: we create a 3D model of the RVE, generate 27 identical copies and arrange them on a $3 \times 3 \times 3$ configuration. We then focus at the center of the super-cell (highlighted in dark gray), which we refer to as the "master" RVE. **(b)** Step B: We impose periodic boundary conditions on each pair (a) and (b) of periodically–located nodes on the boundaries of the "master" RVE. Moreover, we connect the deformation of each node (c) within a "slave" RVE to that of the corresponding node (d) in the "master" RVE. **(c)** Step C: we pressurize the RVE. **(d)** Step D: we subject the pressurized model to 9 independent modes of deformation.

applied pressure is then obtained by monitoring the displacements of the virtual points. Finally, we note that in our analysis $p \leq 101$ kPa – the upper limit corresponding to perfect vacuum conditions and the physical limit of vacuum-based jamming soft robots in standard atmospheric conditions.

Step D: Deformation. In the last step, we subject the pressurized model to 9 independent modes of deformation. To this end, we multiplicatively decompose the macroscopic deformation gradient $\boldsymbol{F}$ into pressurization (Step C) and deformation following a Kroner-Lee decomposition (Kröner, 1959; Lee, 1969)

$$\boldsymbol{F} = \boldsymbol{F}^{\mathrm{d}}.\boldsymbol{F}^{\mathrm{h}}, \tag{3}$$

where $\boldsymbol{F}^{\mathrm{h}}$ is the deformation gradient induced by the applied pressure (Step C) and

$$\boldsymbol{F}^{\mathrm{d}} = F^{d}_{ij}\,\boldsymbol{e}_i\boldsymbol{e}_j, \tag{4}$$

F^{d}_{ij} represents the deformation to be applied in the $\boldsymbol{e}_i\,\boldsymbol{e}_j$ direction. Operationally, for each geometry, we perform 9 separate simulations in which we prescribe a different deformation component F^{d}_{ij} while setting all other components to zero (note that this is accomplished by prescribing the displacement components of the three virtual points). Moreover, to minimize the computational time and avoid recomputing Step C for each deformation case, we use the restart functionality of Abaqus and begin all 9 simulations from the end of Step C.

3. Results

In all our simulations, we capture the mechanical response of the solid components (i.e. layers/fibers) using a linear elastic material with Young's modulus $E = 2$ GPa and Poisson's ratio $\nu = 0.42$ (which are representative values for polypropylene plastic). Furthermore, for the contact at the surfaces of the discrete media, we use the finite sliding contact formulation within Abaqus Standard with a friction coefficient $\mu = 0.6$ and elastic slip tolerance equal to 0.05% of the characteristic element length.

3.1. Layer-based media

We begin by investigating the response of a structure comprising a 1D array of elastic layers of thickness t (see Fig. 1). To capture the response of this system, we choose an RVE comprising two identical rectangular blocks with thickness $0.5t$, width $2t$ and depth $2t$, which are originally at distance $\delta = t/50$ (see Fig. 1a). We first induce the jamming transition by pressurizing the model to $p = 5.05 \times 10^{-5}E$ (corresponding to the maximum attainable vacuum pressure of 101 kPa). We then subject the pressurized super-cell to different independent deformation modes (note that due to symmetry only 5 deformation modes need to be considered for this geometry) and determined the corresponding relationships between nominal stress s_{ij}[2] and the deformation gradient F^{d}_{ij}.

The results reported in Fig. 2a and b show a key feature. For normal modes of deformation (i.e., when we apply F^{d}_{xx}, F^{d}_{yy} and F^{d}_{zz}) and shear in the x-z plane (i.e., when we apply F^{d}_{xz}) the $s_{ij} - F^{d}_{ij}$ response of the layered jammed medium is piecewise linear about the origin (i.e, linear in tension and compression) (see Fig. 2a and b). However, for shear deformations in the x-y and y-x planes (i.e., when we apply F^{d}_{xy} and F^{d}_{yx}), the response is highly nonlinear and features an initial linear regime followed by a region in which the stiffness is significantly reduced (see Fig. 2b). Notably, by performing a set of simulations in which we systematically vary the applied pressure p (while keeping $\mu = 0.6$) and the friction coefficient μ (while keeping p= 101 kPa), we find that the transition between the two regimes occurs when the nominal stress reaches the value of $s_{\mathrm{yield}} = \mu p$ (see Fig. 2c). Therefore, our analysis reveals that the response of the system can be easily controlled by either varying the magnitude of the pressure applied p or by changing the surface properties to vary the friction coefficient μ.

Next, we focus on the (initial) linear response of the medium and investigate the relation between the effective stiffness $\partial s_{ij}/\partial F^{d}_{ij}$ and the elastic material properties of the layers. We find that.

- for any applied shear deformation

$$\left.\frac{\partial s_{ij}}{\partial F^{d}_{ij}}\right|_{F^{d}_{ij}=0} = G = \frac{E}{2(1-\nu)}, \qquad i \neq j, \tag{5}$$

where G denotes the shear modulus of the bulk material;

- for $F_{xx} > 1$ and $F_{zz} > 1$ (i.e., when we apply tension in the x- and z-directions)

$$\frac{\partial s_{xx}}{\partial F^{d}_{xx}} = \frac{\partial s_{zz}}{\partial F^{d}_{zz}} = E, \tag{6}$$

which is the Young's modulus of the bulk material;

- for $F_{yy} > 1$ (i.e., when we apply tension in the y-direction)

$$s_{yy} = 0, \quad \text{and} \quad \frac{\partial s_{yy}}{\partial F^{d}_{yy}} = 0, \tag{7}$$

since no stress (beyond vacuum pressure) is required to separate the layers.

- for $F_{ii} < 1$ (with $i = x,\ y,\ z$ – i.e., when we compress the medium)

$$\frac{\partial s_{xx}}{\partial F^{d}_{xx}} = \frac{\partial s_{yy}}{\partial F^{d}_{yy}} = \frac{\partial s_{zz}}{\partial F^{d}_{zz}} = \frac{E(1-\nu)}{(1+\nu)(1-2\nu)}, \tag{8}$$

which is greater than E for $\nu > 0$ (note that for $\nu = 0$ the effective stiffness reduces to E). This increase in the effective stiffness is due to the fact that under compression, the cross-sectional area of the layers tends to increase for $\nu > 0$. However, since such a change in the cross section of the layers is prevented in our analysis (by explicitly prescribing all components of F^{d}_{ij}), this behavior causes a larger effective stiffness.

Additionally, the results of Fig. 2a and b indicate that, while for normal modes of deformation (i.e., when we apply F^{d}_{xx}, F^{d}_{yy} and F^{d}_{zz}) the response of the structure is different between tension and compression, when a shear deformation is applied to the jammed medium, the nominal stress s_{ij} is an odd function of F^{d}_{ij} and

$$s_{ij}(F^{d}_{ij}) = -s_{ij}(-F^{d}_{ij}), \qquad i \neq j. \tag{9}$$

As such, for the shear modes of deformation in the following analyses, we only consider $F^{d}_{ij} > 0$.

Finally, as shown by the markers in Fig. 2a and b, we repeated our analyses just considering the "master" RVE (i.e., without introducing the "slave" RVEs). The results indicate that, for the material properties and loading conditions considered here, the "master" RVE is sufficient to capture the response in all deformation cases with negligible deviations from analyses in which we also included the "slave" RVEs. To minimize the computational cost of our subsequent FE simulations, we only consider the "master" RVE to analyze the mechanical response of the considered discrete media. However, we note that the super–cell approach accounting for both the "master" and "slave" unit cells is always the most accurate method for any set of geometric and material parameters and loading conditions.

3.2. Fiber-based media

The numerical results of Fig. 2 clearly indicate that the location of

[2] Note that the stress reported in all our results represents the change from the vacuum pressure observed when applying F^{d}_{ij} (i.e. the total stress is $s_{ij}\delta_{ij} + p$, δ_{ij} being the Kronecker delta).

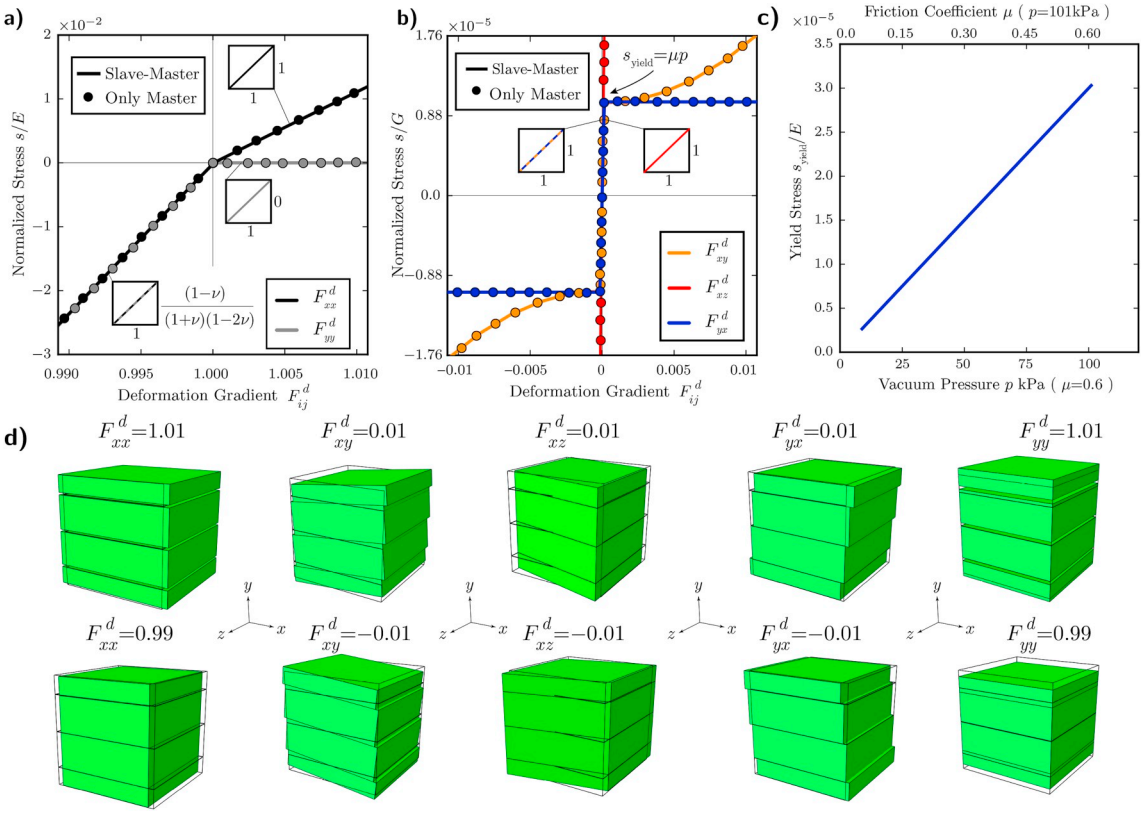

Fig. 2. Layer-based media.(a)–(b) Evolution of the normalized nominal-stress as function of the applied deformation in a jammed RVE for **(a)** F^d_{xx} and F^d_{yy} **(b)** F^d_{xy}, F^d_{xz}, and F^d_{yx}. The jamming transition is triggered by applying $p = 101$ kPa. Solid lines correspond to the results of the super-cell comprising 27 identical RVEs and markers to the results obtained considering only the "master" RVE. Note that because of symmetry, only 5 independent modes of deformation exist, since $F^d_{xx} = F^d_{zz}$, $F^d_{xy} = F^d_{zy}$, $F^d_{xz} = F^d_{zx}$ and $F^d_{yx} = F^d_{yz}$. **(c)** Evolution of the normalized yield stress as a function of the vacuum pressure p (while keeping $\mu = 0.6$) and the friction coefficient μ (while keeping $p = 101$ kPa). **(d)** Snapshots of the super-cell for each of the 5 independent modes of deformation at $F^d_{ij} = \delta_{ij} \pm 0.01$, where δ_{ij} is the Kronecker delta.

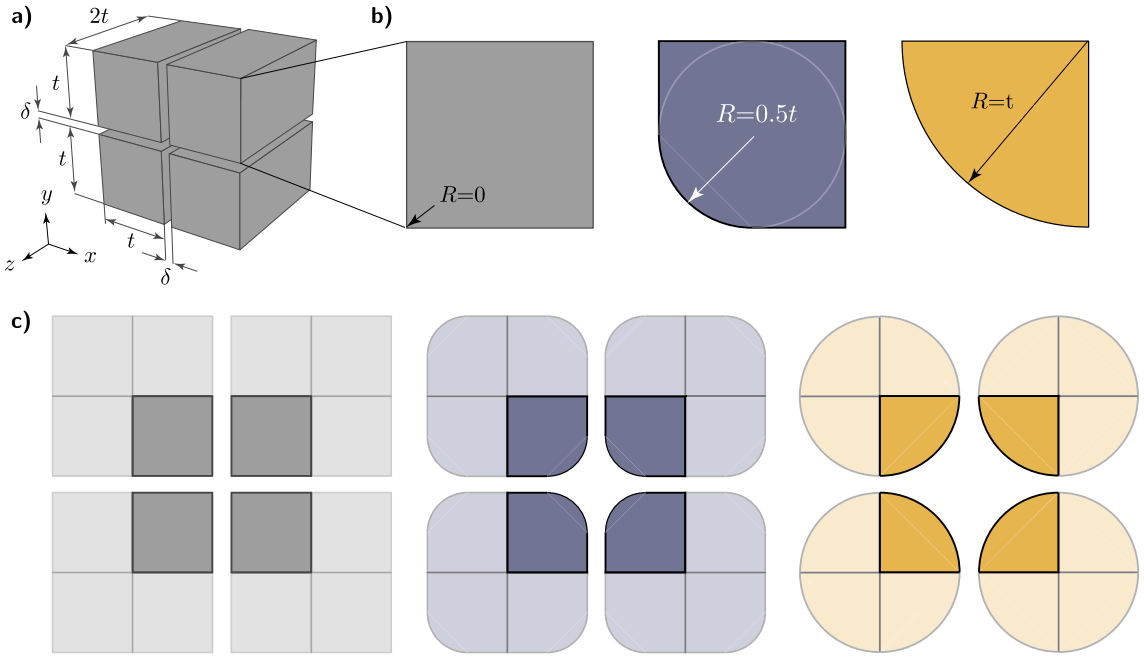

Fig. 3. Fiber-based media – Geometry of square array. (a) Schematic of the RVE for fibers with a square cross section. **(b)** The radius R enables the study of media composed of fibers with different cross sections varying from square ($R = 0$) to fully circular ($R = t$). **(c)** Schematic of the three considered "master" RVEs with fibers arranged in a square packing. The fibers are characterized by $R = 0$ (shown in gray), $R = 0.5t$ (shown in blue) and $R = t$ (shown in orange). (For interpretation of the references to colour in this figure legend, the reader is referred to the Web version of this article.)

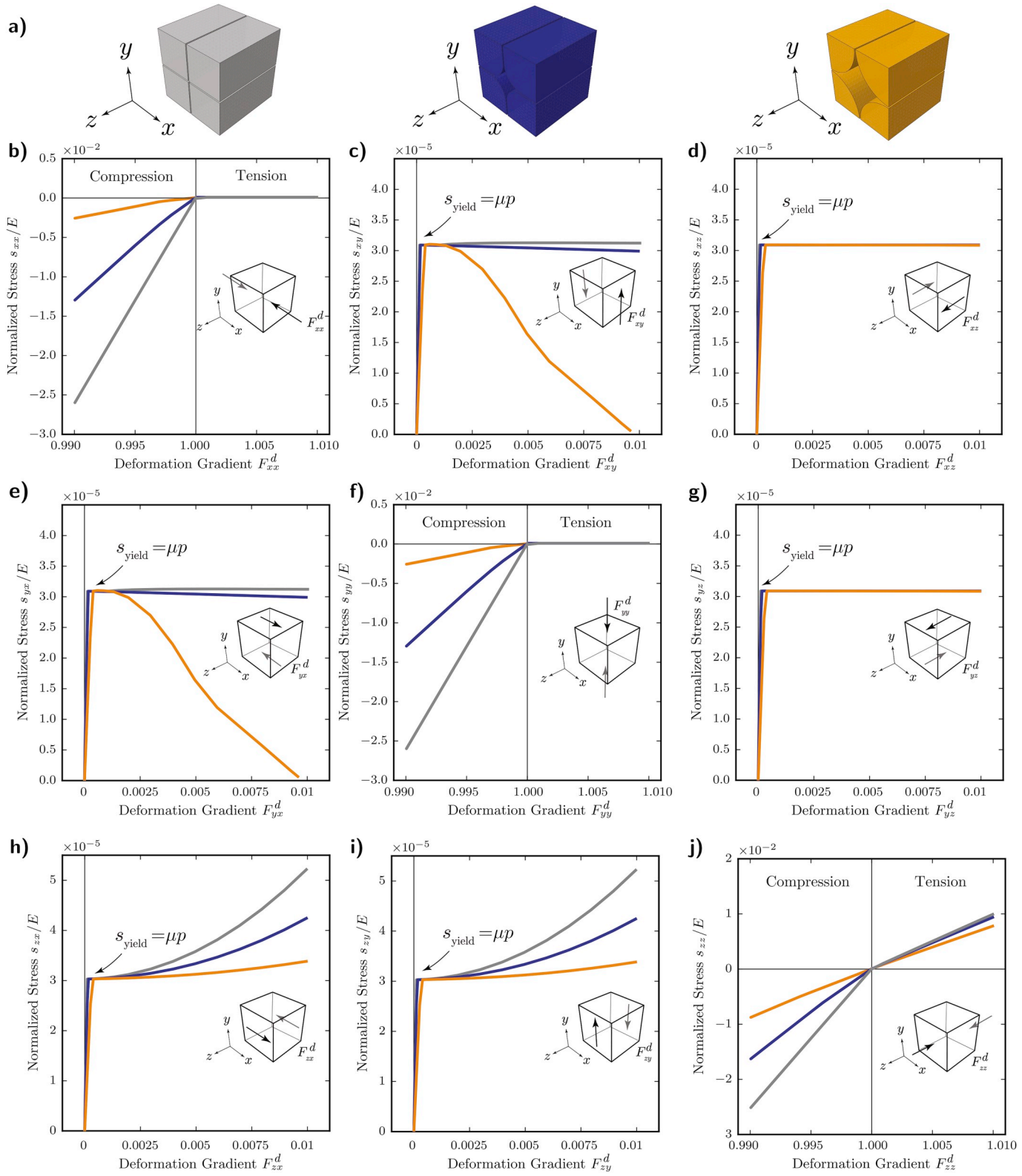

Fig. 4. Fiber-based media – Results for square array. (a) Schematic of the three considered RVEs, corresponding to $R = 0$ (gray), $R = 0.5t$ (blue) and $R = t$ (orange). **(b)–(j)** Relationships between the applied deformation F^d_{ij} and the resulting nominal stress s_{ij} for jammed RVEs initially subjected to $p = 101kPa$. (For interpretation of the references to colour in this figure legend, the reader is referred to the Web version of this article.)

the surfaces along which the discrete elements can slide can directly influence the mechanical response of jammed media. Specifically, for the previously-considered stack of elastic layers, yielding does not occur for shear deformations in the x-z plane, since this mode of deformation does not require relative motion of the layers (see Fig. 2b). To further understand the effect of the location of the sliding surfaces on the response of jammed structures, we consider fiber-based media and focus on the effect of the fiber arrangement, as well as of the fiber cross-section.

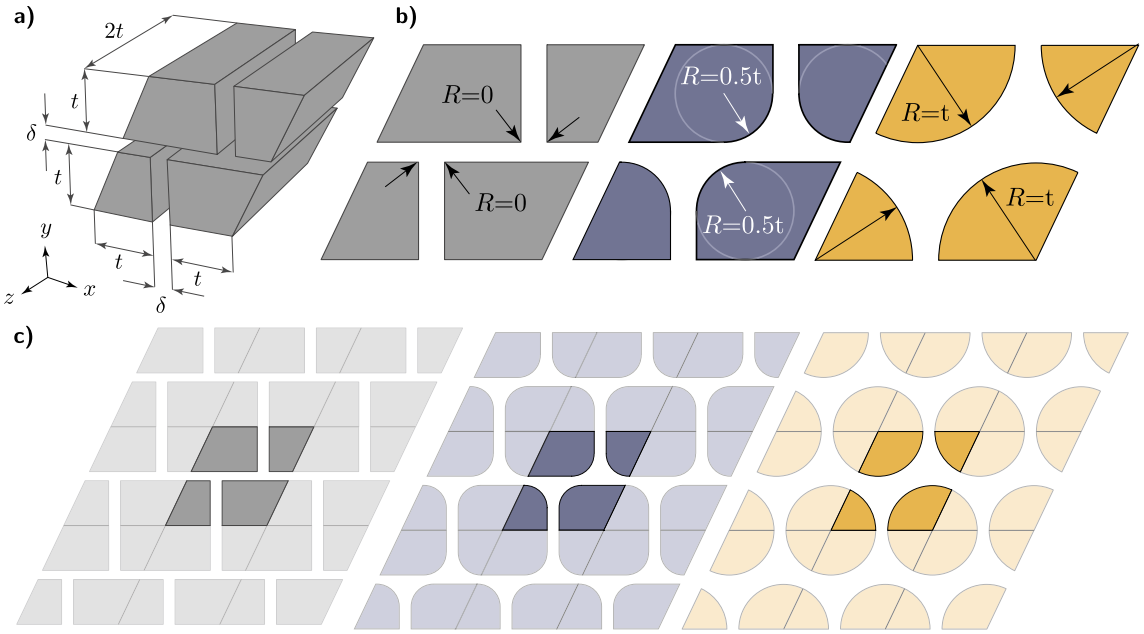

Fig. 5. Fiber-based media – Geometry of staggered array. (a) Schematic of the RVE for fibers with a square cross section. **(b)** The radius R enables the study of media composed of fibers with different cross sections varying from square ($R = 0$) to fully circular ($R = t$). **(c)** Schematic of the three considered "master" RVEs with fibers arranged in a square packing. The fibers are characterized by $R = 0$ (shown in gray), $R = 0.5t$ (shown in blue) and $R = t$ (shown in orange). (For interpretation of the references to colour in this figure legend, the reader is referred to the Web version of this article.)

3.2.1. Square arrangement

We start by considering an infinite array of fibers arranged in a square packing (see Fig. 3a) and introduce the radius R to define their cross-sectional shape (see Fig. 3b), with $R = 0$ corresponding to fibers with a square cross sectional area and $R = t$ corresponding to fully circular fibers with radius t. The RVE for this fiber-based configuration consists of 4 blocks located at a distance $\delta = t/50$ from one another, each representing a quarter of the actual fiber's geometry (see Fig. 3c). In Fig. 4 we report the evolution of the nominal stress s_{ij} as a function of the deformation gradient F^d_{ij} for three jammed RVEs characterized by $R = 0$ (i.e., square fibers), 0.5 (i.e., rounded fibers) and 1 (i.e., circular fibers) in which the jamming transition is triggered by applying $p = 5.05 \times 10^{-5}E$ (corresponding to the maximum attainable vacuum pressure of 101 kPa). By comparing the results of Fig. 4 with those obtained for a layer-based medium (see Fig. 2), we find that the introduction of a square array of fibers qualitatively changes the response of the system when we apply F^d_{xx} (see Fig. 4b) and F^d_{xz} (see Fig. 4d). Specifically, when we consider a square array of fibers and superimpose the deformation $F^d_{xx}>1$, the effective stiffness of the jammed medium vanishes (see Fig. 4b). Moreover, the shear deformation induced by F^d_{xz} causes all three fiber-based structures to yield at $s_{\text{yield}} = \mu p$, fully altering the no-yielding behavior of the laminar medium under x-z shear (see Figs. 2b and 4d).

The results of Fig. 4 also indicate that the initial stiffness of the medium depends linearly on the cross–sectional area of the fibers as expected. While for perfectly square fibers (i.e., $R = 0$), we recover the stiffness measured for layer-based media, larger values of R result in a more compliant initial response. Lastly, it is important to point out that variations in the cross section of the fibers play a significant role for in-plane shear modes of deformation (i.e., for F^d_{xy} and F^d_{yx}). For these deformation modes, larger values of the radius R lead to a pronounced stiffness reduction pre- and post-yield, and in the extreme case of circular fibers ($R = t$), result in a totally unstable post-yielding response (see Fig. 4c and e). In contrast, out-of-plane shear modes of deformation (i.e., for F^d_{xy} and F^d_{yz}) are almost immune to variations in the cross section of the fibers (see Fig. 4d and g).

3.2.2. Staggered arrangement

Next, to investigate the effect of the arrangement of the fibers on the mechanical response of the medium, we consider elastic fibers with the same cross section as those presented in Figs. 3 and 4, but arranged in a staggered configuration (see Fig. 5). Such an arrangement can be obtained from the previously-considered square packing by simply translating every other row of fibers by one half of the fiber's width/diameter t. The corresponding RVE is obtained by cutting the staggered fiber-based infinite medium along straight lines that connect the centers of four neighbouring fibers and comprises 4 blocks located at a distance $\delta = t/50$ from one another (see Fig. 5b and c). The results reported in Fig. 6 indicate that, independently of the cross section of the fibers, the relationship between the nominal stress and deformation gradient for normal modes of deformation (i.e., F^d_{xx}, F^d_{yy} and F^d_{zz}) is unaltered when transitioning from a square-to a staggered-fiber packing (see Fig. 6b, f and j). This is because the results are expressed in terms of $\boldsymbol{F}^d$, while all discrepancies caused by differences in the packing configuration are captured by $\boldsymbol{F}^h$. Moreover, the simulations also show that the different fiber arrangements do not affect the response of the medium for out-of-plane shear deformations (i.e., for F^d_{xz}, F^d_{yz}, F^d_{zx} and F^d_{zy} – see Fig. 6d, g, h and i). In contrast, the staggered configuration dramatically changes the in-plane shear response (i.e., F^d_{xy} and F^d_{yx} – see Fig. 6c and e). Particularly, for the case of circular fibers (i.e., for $R = t$), the stress-deformation relationship exhibits no yield point when we apply either F^d_{xy} or F^d_{yx}. Differently, for $R = 0$ and $R = 0.5t$, the s-F^d relationship maintains the yield point at $s_{\text{yield}} = \mu p$, but the responses resulting from F^d_{xy} and F^d_{yx} are no longer identical with a post-yield strain-stiffening emerging for F^d_{xy}.

4. Conclusions

In summary, we have introduced an effective FE-based numerical tool to investigate the response of discrete infinite media undergoing a jamming transition. The proposed numerical approach enables us not only to predict the highly nonlinear response of these systems, but also to determine how the geometry, arrangement and frictional properties of the discrete constituents affect the presence and location of the yield point. While in this study we have focused on layer-based and fiber-

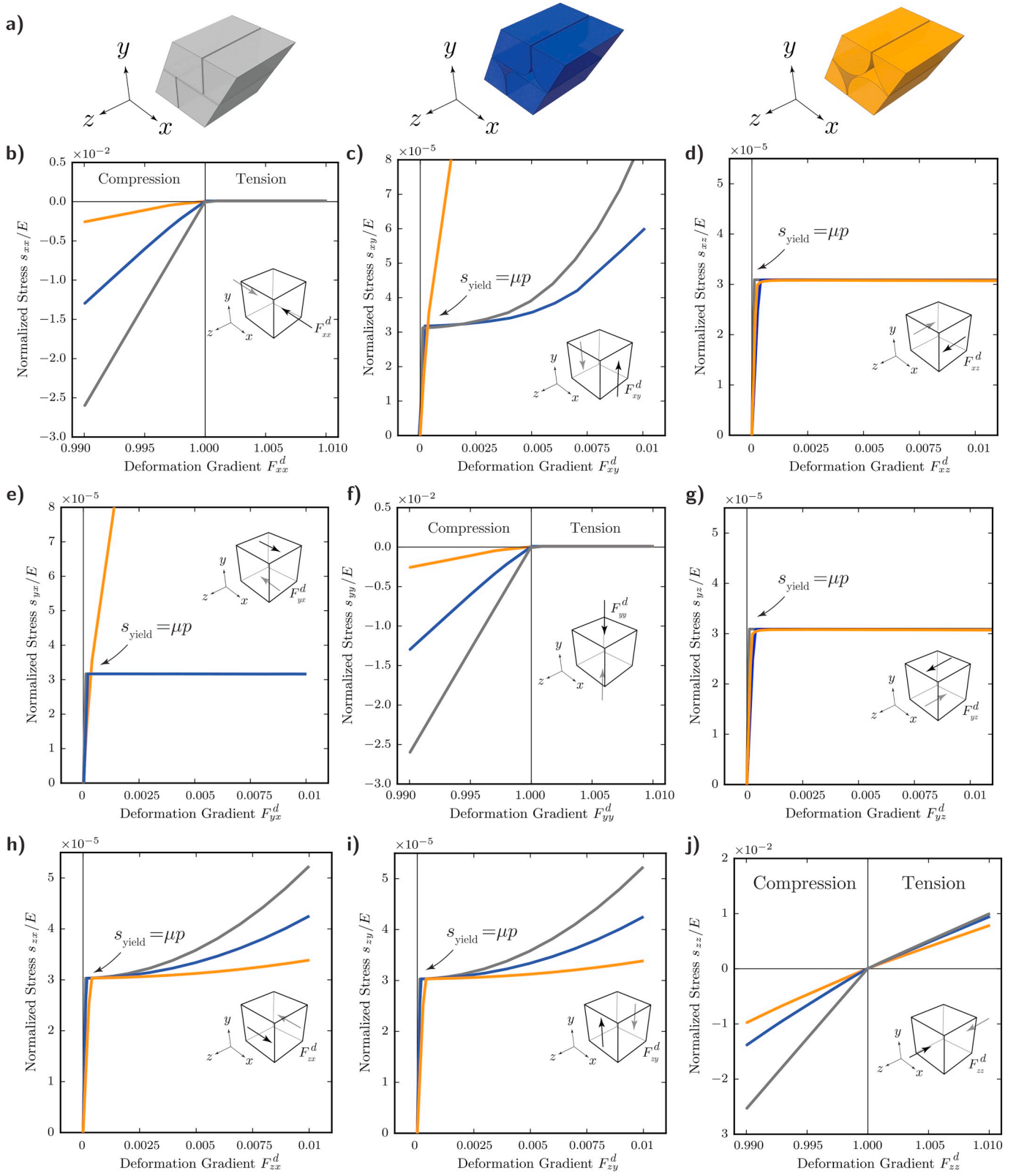

Fig. 6. Fiber-based media – Results for staggered array. (a) Schematic of the three considered RVEs, corresponding to $R = 0$ (gray), $R = 0.5t$ (blue) and $R = t$ (orange). **(b)–(j)** Relationships between the applied deformation F_{ij} and the resulting nominal stress s_{ij} for jammed RVEs initially subjected to $p = 101kPa$. (For interpretation of the references to colour in this figure legend, the reader is referred to the Web version of this article.)

based media, our approach can be readily extended to any packing of granular media or arbitrarily-shaped elements. Moreover, despite the fact that our analysis focuses on infinite periodic structures, we believe the insights gained can be generalized directly to the design of finite systems. As such, this work serves as a platform to accelerate the design of soft robotic devices relying on the jamming transition. In addition, it provides a unified toolkit to investigate promising combinations of jamming media (i.e. fiber-layer jamming composites, granular-layer

jamming composites, etc., as proposed in (Narang, 2018)), facilitating their design and minimizing the number of experiments required.

Acknowledgements

Funding was provided by the National Science Foundation National Robotics Initiative Grant CMMI-1637838 and the National Science Foundation Graduate Research Fellowship Award 1122374. N. Vasios acknowledges Zhihang Qin, who during his time as a visiting student at Harvard University contributed to the development of the Abaqus Python scripts for the square- and staggered-fiber jamming geometries.

Appendix A. Supplementary data

Supplementary data to this article can be found online at https://doi.org/10.1016/j.euromechsol.2019.02.002.

References

Bertoldi, K., Boyce, M.C., 2008. Wave propagation and instabilities in monolithic and periodically structured elastomeric materials undergoing large deformations. Phys. Rev. B 78, 184107.
Brown, E., Rodenberg, N., Amend, J., Mozeika, A., Steltz, E., Zakin, M.R., Lipson, H., Jaeger, H.M., 2010. Universal robotic gripper based on the jamming of granular material. Proc. Natl. Acad. Sci. 107, 18809–18814.
Danielsson, M., Parks, D., Boyce, M., 2002. Three-dimensional micromechanical modeling of voided polymeric materials. J. Mech. Phys. Solid. 50, 351–379.
Dian, Y., V. M. S, JuHee, S., Bobak, M., Christoph, K., Benjamin, L., Fatemeh, K., Elton, L., Zhigang, S., W. G. M, 2016. Buckling pneumatic linear actuators inspired by muscle. Adv. Mater. Technol. 1, 1600055.
Henann, D.L., Kamrin, K., 2013. A predictive, size-dependent continuum model for dense granular flows. Proc. Natl. Acad. Sci. 110, 6730–6735.
Henann, D.L., Kamrin, K., 2014. Continuum modeling of secondary rheology in dense granular materials. Phys. Rev. Lett. 113, 178001.
Ilievski, F., Mazzeo, A.D., Shepherd, R.F., Chen, X., Whitesides, G.M., 2011. Soft robotics for chemists. Angew. Chem. Int. Ed. 50, 1890–1895.
Jaeger, H.M., 2015. Celebrating soft matters 10th anniversary: toward jamming by design. Soft Matter 11, 12–27.
Kawamura, S., Yamamoto, T., Ishida, D., Ogata, T., Nakayama, Y., Tabata, O., Sugiyama, S., 2002. Development of passive elements with variable mechanical impedance for wearable robots. In: Proceedings 2002 IEEE International Conference on Robotics and Automation (Cat. No. 02CH37292), volume 1pp. 248–253.
Kim, S., Laschi, C., Trimmer, B., 2013a. Soft robotics: a bioinspired evolution in robotics. Trends Biotechnol. 31, 287–294.
Kim, Y., Cheng, S., Kim, S., Iagnemma, K., 2013b. A novel layer jamming mechanism with tunable stiffness capability for minimally invasive surgery. IEEE Trans. Robot. 29, 1031–1042.
Kröner, E., 1959. Allgemeine Kontinuumstheorie der Versetzungen und Eigenspannungen. Arch. Ration. Mech. Anal. 4, 273–334.
Laschi, C., Mazzolai, B., Cianchetti, M., 2016. Soft robotics: technologies and systems pushing the boundaries of robot abilities. Sci. Robot. 1.
Lee, E.H., 1969. Elastic-plastic deformation at finite strains. J. Appl. Mech. 36.
Liu, A.J., Nagel, S.R., 2010. The jamming transition and the marginally jammed solid. Ann. Rev. Condens. Matter. Phys. 1, 347–369.
Majidi, C., 2014. Soft robotics: a perspective—current trends and prospects for the future. Soft Robot. 1, 5–11.
Manti, M., Cacucciolo, V., Cianchetti, M., 2016. Stiffening in soft robotics: a review of the state of the art. IEEE Robot. Autom. Mag. 23, 93–106.
Narang, Y.S., 2018. Achieving Mechanical Versatility in Robots and Structures through Laminar Jamming. Ph.D. thesis. Harvard University.
Narang, Y.S., Vlassak, J.J., Howe, R.D., 2018a. Mechanically versatile soft machines through laminar jamming. Adv. Funct. Mater. 28, 1707136.
Narang, Y.S., Degirmenci, A., Vlassak, J.J., Howe, R.D., 2018b. Transforming the dynamic response of robotic structures and systems through laminar jamming. Robot. Automat. Lett. 3, 688–695.
Ou, J., Yao, L., Tauber, D., Steimle, J., Niiyama, R., Ishii, H., 2013. jamsheets: thin interfaces with tunable stiffness enabled by layer jamming. In: Proceedings of the 8th International Conference on Tangible, Embedded and Embodied Interaction. TEI '14, ACM, New York, NY, USA, pp. 65–72.
Polygerinos, P., Correll, N., Morin, S.A., Mosadegh, B., Onal, C.D., Petersen, K., Cianchetti, M., Tolley, M.T., Shepherd, R.F., 2017. Soft robotics: review of fluid-driven intrinsically soft devices; manufacturing, sensing, control, and applications in human-robot interaction. Adv. Eng. Mater. 1700016.
Rus, D., Tolley, M.T., 2015. Design, fabrication and control of soft robots. Nature 521, 467.
Rycroft, C.H., Bazant, M.Z., Grest, G.S., Landry, J.W., 2006. Dynamics of random packings in granular flow. Phys. Rev. E 73, 051306.
Shepherd, R.F., Ilievski, F., Choi, W., Morin, S.A., Stokes, A.A., Mazzeo, A.D., Chen, X., Wang, M., Whitesides, G.M., 2011. Multigait soft robot. Proc. Natl. Acad. Sci. 108, 20400–20403.
Trivedi, D., Rahn, C.D., Kier, W.M., Walker, I.D., 2008. Soft robotics: biological inspiration, state of the art, and future research. Appl. Bionics Biomechanics 3, 99–117.
Zhao, H., O'Brien, K., Li, S., Shepherd, R.F., 2016. Optoelectronically innervated soft prosthetic hand via stretchable optical waveguides. Sci. Robot. 1.